RESEARCH ARTICLE | JUNE 12 2023

Short-to long-term deformation behavior of glassy polymers under cyclic uniaxial, torsional, and multiaxial loads

Sami Holopainen ✉; Thierry Barriere; Xavier Gabrion; Abel Cherouat

AIP Conf. Proc. 2848, 020028 (2023)
https://doi.org/10.1063/5.0145488

Short- to Long-Term Deformation Behavior of Glassy Polymers under Cyclic Uniaxial, Torsional, and Multiaxial Loads

Sami Holopainen[1, a)], Thierry Barriere[2, b)], Xavier Gabrion[2, c)], and Abel Cherouat[3, d)]

[1)] *Tampere University, Department of Civil Engineering, FI-33014 Tampere, Finland.*
[2)] *Univ. Bourgogne Franche-Comt ´e, FEMTO-ST Institute, CNRS/UFC/ENSMM/UTBM, Department of Applied Mechanics, 25000 BESANCON-FR, France.*
[3)] *Univ. Technology of Troyes, Laboratory of Automatic Generation of Meshing and Advanced Methods (GAMMA3), Troyes, France.*

[a)] *Corresponding author: sami.holopainen@tuni.fi*
[b)] *Electronic mail: thierry.barriere@univ-fcomte.fr*
[c)] *Electronic mail: xavier.gabrion@ens2m.fr*
[d)] *Electronic mail: abel.cherouat@utt.fr*

Abstract. Despite the popularity of glassy polymers, the research of their short- to long-term fatigue resistance has been considerably limited to date. In this research, both an enhanced molding equipment and a model are proposed to investigate the resistance of glassy polymers (polycarbonate, PC) under cyclic fatigue loads. Two failure mechanisms consider the low-cycle and high-cycle regimes, respectively: plastically induced (including the effect of free volume) and fatigue. Therefore, the proposed model is history dependent. Contrast to state-of-the-art models, the proposed model is capable to simulate the experimentally observed ultralow- to high-cycle fatigue life, suggesting that the model is a valid tool for simulating time-consuming and costly tests. It is noteworthy that the predicted progress of material damage was found to resemble the observed development of accumulated void volume. The damage development significantly affected the onset and growth of tertiary cyclic creep and thus, the length of fatigue life. The amorphous microstructure also appeared to firmly resist failure under torsion and better than under uniaxial loads.

INTRODUCTION

The widespread use of amorphous polymers (APs) in R&D is owing to their favorable properties, e.g., cheap price, optical clearness, and impact toughness. Therefore APs represent highly important technological materials from engineering components (in vehicles, sporting goods etc.) to aeronautic equipment (e.g., the cockpit canopy of the Lockheed Martin F-22 Raptor fighter) [1, 2, 3, 4]. APs are also used as ingredients to improve the toughness of biopolymers [1, 5]. However, all these applications may suffer from failure under cyclic loading processes and therefor it is worth investigating and testing the fatigue resistance. Such tests are costly, and thus, it is worth developing capable models to simulate resource-intensive tests and to facilitate the development of more resistant materials [6] including APs.

The Boyce-Parks-Argon (BPA) constitutive model [7], probably the most established model in the field, is suitable for predicting the large deformation of APs. However, the BPA model is elastic-viscoplastic and thus is limited by its inaccurate predictions of the yield strain, unloading response, recovery, and creep observed in corresponding tests [8, 9, 10]. Considering APs, both viscoelastic and viscoplastic elements are required to accurately predict these elements [11, 12], and thus the cyclic deformation behavior [13, 14]. Nevertheless, only a few models comprise both these elements, despite being demonstrated under solely 1D loads [10, 15, 16, 17, 18].

In addition to the plastically induced failure, material may also show a fatigue damage mechanism [19, 20]. However, no main consensus can be found from the literature for modeling fatigue of APs [20]. The majority of the research has been focused on low-cycle fatigue [21, 22], and regarding longer fatigue lives and ratcheting, the research has been concentrated on uniaxial cyclic loadings [2, 10, 18, 23, 24, 25].

Analysis of entire structural components for long fatigue lives demands a great deal of computational resources. Therefore, the analysis was first done by using a simple approach for the entire structure. The isotropic ductile damage model introduced by Lemaitre and Chaboche [26] (the $[1-D]$ concept) was coupled with the viscoelastic-plastic Johnson-Cook (JC) constitutive model [27], and the coupled model was implemented in Abaqus/Explicit [27, 28]. The remeshing was conducted with linear tetrahedra elements. Although the applied model with the remeshing concept [28] is robust, it seemed to exaggerate fatigue life; 60,000 cycles, while the measured fatigue lives corresponded to approximately 20,000 cycles. In addition, the JC model and the damage model applied are empirical and do not incorporate the specific characteristics of amorphous microstructure observed under long-term cyclic loadings.

The viscoelastic-viscoplastic model for APs introduced in Barriere et al. [10] has been shown to be accurate under multiaxial long-term cyclic loading processes [14], and it was used in this research. However, this model is limited

Advances in Fracture and Damage Mechanics XX
AIP Conf. Proc. 2848, 020028-1–020028-9; https://doi.org/10.1063/5.0145488
Published by AIP Publishing. 978-0-7354-4548-2/$30.00

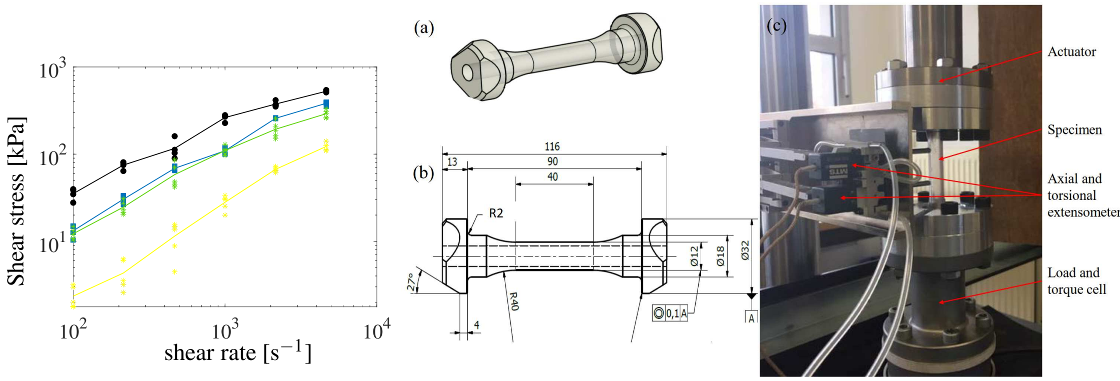

FIGURE 1. Shear rate vs shear stress and temperature for PC at 260°C (black), 280°C (blue), 300°C (green), 320°C (yellow) (left). Shape (a) and dimension [mm] (b) of the torsion specimen according to the standard [31] (middle). The testing setup (c) (right). Extracted from [33] (doi.org/10.1016/j.ijplas.2021.103106) under the CC-BY-NC-ND license: www.elsevier.com/about/policies/copyright.

in that it underestimates the shear ratcheting strain, especially that prior to rupture. The rigidity of the model in shear is owing to the applied eight-chain model [7], which has been evidenced to be quite rigid under shear loadings [29, 30]. On this basis, an improvement of the model was proposed. A fundamental fatigue damage model for predicting fatigue live of APs under different stress modes and levels proposed in Barriere et al. [14] (contrast to cycle-counting approaches) was used, capable of predicting fatigue life from the ultralow-cycle regime (fewer than one hundred cycles) to the high-cycle regime (hundreds of thousands of cycles). Based on the results of both testing and modeling, the effects of the load path, loading rate, and stress amplitude on the cyclic deformation behavior (ratcheting) and fatigue life are demonstrated.

PREPARATION OF SPECIMENS

A thermoplastic mold with suitable die cavities (based on ASME standard) was fabricated for the tests. The injection tests were realized with a dry PC Lexan® 223R granulate. The shear rate vs shear stress and temperature from 260°C to 320°C, which responses are used to describe the capability of polymers for injection molding, were measured using a standard capillary rheometer having a die cavity of 1 mm in diameter and 16 mm in length, see Fig. 1. The so-called pseudoplastic behavior was recognized, that is, it can be deduced that the PC applied is prone to temperature and therefore challenging to inject. Therefore, to product specimens without remarkable external defects, the runner and gate size of the mold were increased. Then, the differential scanning calorimetry (DSC) results verified that the injection-molded specimens had the same physical properties as the original PC granulate. Moreover, no significant flaws in the specimens was observed based on the X-ray tomography and Werth video-check applied. The high quality of the final shape was further verified by employing optic 3D metrology (Alicona analyzer).

Instron® Electropulse E10000 machine having a load capacity of 10 kN and a displacement capacity of ± 30 mm was used in the tests. The load cell capacity and the maximum angle of the machine for torsion were ±100 Nm and 135°, respectively.

TESTS

The following tests were performed: [1] displacement-controlled quasi-static and monotonic tests at the strain rates of $\dot{\varepsilon} = 0.001$, 0.01, and 0.1 s^{-1} until rupture, [2] cyclic force-controlled tests at $f = 5$ Hz (sinusoidal) until rupture at $R = 0.1$ (the maximum stress values were 25, 37.5, 50, 75, 90, and 97 % of the peak yield stress, 60 MPa).

The test set [1] was performed to observe the yield stress and strain, and softening at large strains, see [14]. The test set [2] was designed to investigate the influence of the maximum stress (incl. the mean stress and amplitude) on ratcheting and fatigue life.

The force F and the corresponding axial elongation u were recorded by the testing machine. Furthermore, the axial elongation was measured by an extensometer (glued onto the surface of the specimens to avoid sliding), and the results of the machine and extensometer were similar. The strain was calculated as $\varepsilon := u/L$, where L is the gauge length of the extensometer used. The so called first Piola-Kirchhoff stress $\sigma := F/A$ was used because it is easy to measure and calculate: force F divided by the original undeformed cross-sectional area A. The error in relation to the true Cauchy stress is small because the change in the cross-sectional area before and after the tests was small (the cyclic strains were less than 10 %).

The following force-controlled tests were performed: [1] quasi-static torsion using the torque speed 1 Nms^{-1} until rupture and [2] cyclic tests at $R = 0.1$ and $f = 1$ Hz (sinusoidal) until rupture (the maximum shear stresses were 30 %, 50 %, 65 %, 75 %, 82.5 %, and 90 % of the ultimate shear strength, 40 MPa). The test set [1] enabled the observation of the shear yield strain and the corresponding stress and softening at large strains. In addition to the machine, the torsion angle was measured by the extensometer (firmly glued onto the surface of the specimens). The shear stress and strain were defined as: $\tau = 16T/\pi(d_\mathrm{o}^2 - d_\mathrm{i}^2)(d_\mathrm{o} + d_\mathrm{i})$ and $\gamma = d_\mathrm{o}\theta/2L_\mathrm{g}$, where T denotes the torque, $d_\mathrm{o} = 12$ mm and $d_\mathrm{i} = 9$ mm are the outer and inner diameters, respectively, θ is the angle in radians, and $L_\mathrm{g} = 40$ mm is the gauge length of the specimens.

This test set was performed to study the effects of different multiaxial load paths on the ratcheting deformation and fatigue life. The applied load-controlled load paths are shown in Fig. 5. The duration of each cycle was 20 seconds, that is, the frequency of 0.05 Hz was used. The torsional test specimens were used, and the axial elongation, axial force, torque, and the torsion angle were recorded by the testing machine. The axial elongation and torsion angle were also measured by the extensometer. The axial stress was calculated as $\sigma = 4F/\pi(d_\mathrm{o}^2 - d_\mathrm{i}^2)$.

MODELING

Plastic deformation

The evolution of the plastic deformation proposed in the closest state-of-the-art model [15] has not been designated for torsion and multiaxial loads and is therefore inaccurate under such load conditions [14]. For this reason, the following improved model is proposed:

$$\dot{\gamma}_\mathrm{ij}^\mathrm{vp} = \dot{v}_0\Big(\frac{\tau^{(1)}}{s^{(1)} - 1/3\alpha I_1 + F(I_1, I_2; \alpha_k)}\Big)^{1/\mathrm{m}_0} \geq 0, \tag{1}$$

where $\dot{v}_0$, m_0, and α denote the material parameters, $s^{(1)}$ is an internal state variable (representing the molecular resistance to plastic shear flow [15]), $I_1 = \mathrm{tr}\,(\boldsymbol{\sigma} - \boldsymbol{\beta}) = \mathrm{tr}\,(\tilde{\boldsymbol{\sigma}}) = \mathrm{tr}\,(\boldsymbol{\sigma})$ is the first invariant indicating pressure ($\boldsymbol{\beta}$ is the traceless deviatoric backstress [10, 15, 32]), $I_2 = 1/2((\mathrm{tr}\,\tilde{\boldsymbol{\sigma}})^2 - \mathrm{tr}\,(\tilde{\boldsymbol{\sigma}}^2))$ is the second invariant, and $\tau^{(1)} = \sqrt{\mathrm{tr}\,(\tilde{\boldsymbol{\sigma}}^2)/2}$ is the equivalent reduced stress. F is the function representing additional molecular resistance to plastic shear flow; α_k, where $k = 1...8$, are positive material parameters. Based on the experimental data, the two different values $\dot{\gamma}_\mathrm{ii}^\mathrm{vp} = \dot{\gamma}_\sigma^\mathrm{vp}$ for tension/compression and $\dot{\gamma}_\mathrm{ij}^\mathrm{vp} = \dot{\gamma}_\tau^\mathrm{vp}$ for shear $i \neq j$, where $i, j = 1, 2, 3$, are considered sufficient under multiaxial loads. The viscoplastic flow rule is given by $\boldsymbol{D}^\mathrm{vp} = (\dot{\gamma}_\sigma^\mathrm{vp}\tilde{\boldsymbol{\sigma}}_\sigma/\tau^{(1)} + \dot{\gamma}_\tau^\mathrm{vp}\tilde{\boldsymbol{\sigma}}_\tau/\tau^{(1)})/2$, where $\tilde{\boldsymbol{\sigma}}_\sigma$ and $\tilde{\boldsymbol{\sigma}}_\tau$ include the diagonal and non-diagonal components of $\tilde{\boldsymbol{\sigma}}$ [10]. The equivalent rate of the plastic deformation including the evolution of the internal, scalar variables $s^{(1)}$ and φ (free volume) [10] is given by $\dot{\gamma}^\mathrm{vp} = \sqrt{2\,\mathrm{tr}\,((\boldsymbol{D}^\mathrm{vp})^2)}$. The function

$$F = e^{-\alpha_1\bar{I}_2}((\alpha_{2,\mathrm{s}}e^{\alpha_4\bar{I}_1}I_2^2 - \alpha_{5,\mathrm{s}})(1 - e^{-\xi I_1^2\bar{I}_2}) - \alpha_7(1 - e^{-\bar{I}_2}) + \alpha_8\bar{I}_2) \tag{2}$$

targets at improving the accuracy of the plastic deformation in (1) under different stress modes and levels [33]. The parameters used are α_k, where $k = 1, 4, 7, 8$. Furthermore, for $\dot{\gamma}_\sigma^\mathrm{vp}$ (axial deformations, $s = 1 = \sigma$) and $\dot{\gamma}_\tau^\mathrm{vp}$ (shear, $s = 2 = \tau$), defined before, the parameters $\alpha_{2,\mathrm{s}}$ and $\alpha_{5,\mathrm{s}}$, where $s = 1, 2$, are different, that is, the total number of parameters k is eight. The constant $\xi = 10^{-5}$ MPa^{-4} is a sufficiently small number for the function F to be smooth at low stresses. It is assumed that $\bar{I}_1 = \sqrt{I_1^2}$ and $\bar{I}_2 = \sqrt{I_2^2}$ are better estimates than I_1 and I_2 especially under compression.

The saturation value of $s^{(1)}$ is

$$\tilde{s}^{(1)} = s_\mathrm{sv}(1 + b(I_1, I_2; b_k)(\varphi_\mathrm{sv} - \varphi(g_0(I_1, I_2; g_k))) > 0, \tag{3}$$

where s_sv and φ_sv are the original model parameters [15] and b_k, where $k = 1, ..., 4$, and g_k, where $k = 1...6$ are additional parameters (determined from torsional and multiaxial tests). The evolution of the free volume is given by [10], that is,

$$\dot{\varphi} = g_0(s^{(1)}/s_\mathrm{cv} - 1)\dot{\gamma}^\mathrm{vp} > 0.$$

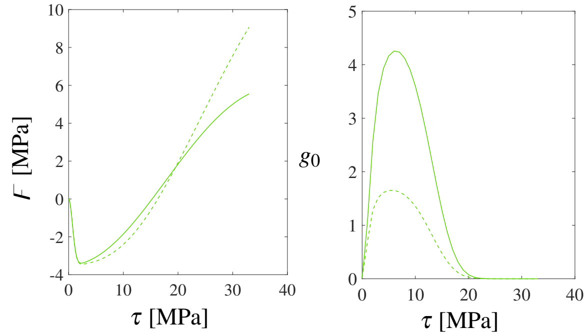

FIGURE 2. Illustration of the function $\mathcal{F}$ (left). Solid and dashed curves are for $\sigma = 0$ MPa (torsion) and $\sigma = 10$ MPa (multiaxial load). Illustration of g_0 (right). Solid and dashed curves are for $\sigma = 20$ MPa and $\sigma = 30$ MPa, respectively. The symbols σ and τ indicate the true axial and shear stresses. Extracted from [33].

It was observed that the constant parameters g_0 and b, which are used in the preceding models to predict uniaxial deformation behavior [10, 15], are insufficient for torsion and multiaxial loads, and therefore

$$g_0 = (e^{-g_1 I_2^2}((1-g_2 I_1^2)\bar{I}_2/g_3 - g_4) + g_5 e^{-\xi I_2^2})/(1+g_6 I_1^2 \bar{I}_2) > 0 \tag{4}$$

is proposed [33]; g_k, where $k = 1,...,6$, are material parameters. The constant $\xi = 10^{-5}$ MPa^{-4} is a sufficiently small number for the function g_0 to be smooth at small stresses. Under uniaxial tension, $g_0 = g_5 - g_4 > 0$ (constant) for adjusting softening [10, 15]. The lower the value of g_0, the greater the variable $s^{(1)}$ and its saturation value restraining the plastic deformation according to (1). The function b in (3) is defined as

$$b = e^{-b_2 \bar{I}_2}(1+b_3 I_1^2 \bar{I}_2)\bar{I}_2/b_4 + b_1 e^{-\bar{I}_2} > 0, \tag{5}$$

where b_k, $k = 1,...,4$, are material parameters [33]. Under uniaxial loads, $b = b_1$ (constant) adjusting the peak yield stress and subsequent softening [15].

The functions $\mathcal{F}$ and g_0 (the shape of b is similar to that of $\mathcal{F}$) are demonstrated in Fig. 2. In accordance with the function $\mathcal{F}$, the function b tends to prevent the evolution of plastic deformation (1) at high shear stresses (high b increases the saturation value (3) and the variable $s^{(1)}$) and enhance it when the shear stress is small. These functions are discussed in detail in Holopainen et al. [33]. They approach the values used in the Anand and Ames model [15] as the shear stress decreases to zero (and $\dot{\gamma}_{ij}^{vp}$ in (1) approaches $\dot{\gamma}^{vp}$). Thereby, the number of additional parameters needed in these functions is reduced to 16. Although the total number of parameters (original 18 + added 16 = 34) needed to capture the complex deformation behavior under different loadings is rather large, almost the same number is needed in the closest state-of-the-art models to model the uniaxial loading alone [15, 17, 18]. All the parameter values are presented in Table 1. The first 18 parameters were calibrated to one monotonic and one cyclic uniaxial data [10]. The remaining parameters for plasticity and fatigue were calibrated to torsional and multiaxial ratcheting loadings. The final values of α_1, α_7, α_8, g_1, g_3, g_4, b_2, and b_4 (eight parameters for shearing) were defined by least squares fitting of the targeted torsion data ($R = 0.1$) at different maximum stress levels of 30 %, 50 %, 75 %, and 82.5 % of the observed ultimate shear strength (40 MPa). The remaining eight parameters, $\alpha_{2,1}$, $\alpha_{2,2}$, α_4, $\alpha_{5,1}$, $\alpha_{5,2}$, g_2, g_6, and b_3 for multiaxial loads, were adjusted using least squares fitting to the data corresponding to combined tension and torsion (the squared and butterfly-type loads) when the maximum stresses were 30 % and 50 % of their strengths. In summary, the additional 16 parameters were determined from eight tests (the order just presented was applied: first torsion and then multiaxial loads with the increasing stress levels).

Fatigue life

A unified fatigue model that is suitable for both high cycle fatigue (HCF) and low cycle fatigue (LCF) regimes under various loading modes is used [33]. This continuum-based fatigue model is an extension of the Ottosen et al. model [34] for HCF of metals, whose model is based on the concept of an evolving damage variable ($0 \leq D \leq 1$) and an endurance surface $\beta = 0$ moving in stress space. The prerequisite is the existence of an asymptotical extreme of lifetime, i.e., the endurance limit, and the fatigue under this limit is extinguished. Unlike in most established

TABLE 1. Constitutive model and fatigue model parameters for the PC used [33].

Elastic and viscoelastic parameters									
Parameter	E	ν	$\dot{v}_0$	α	m_1	$s^{(2)}$	$c_\mathrm{A}\cdot10^{-6}$	$\mu_\mathrm{A,sat}$	μ_A^0
Unit	MPa		s^{-1}			MPa	MPa	MPa	MPa
Value	2000	0.44	0.031	0.204	0.19	12	4.5	2500	8000
Viscoplastic parameters									
Parameter	s_0	m_0	C_R	N	h_0	b	g_0	s_cv	φ_cv
Unit	MPa		MPa		MPa			MPa	
Value	28.0	0.037	14.0	1.65	3500	600	0.014	26.5	0.0013
Parameter	$\alpha_1\cdot10^4$	$\alpha_{2,1}\cdot10^9$	$\alpha_{2,2}\cdot10^9$	α_4	$\alpha_{5,1}$	$\alpha_{5,2}$	α_7	α_8	$b_2\cdot10^4$
Unit	MPa^{-2}	MPa^{-3}	MPa^{-3}	MPa^{-1}	MPa	MPa	MPa	MPa^{-1}	MPa^{-2}
Value	7.7	13	1.8	0.6	2.0	1.0	3.5	0.015	7.0
Parameter	$b_3\cdot10^6$	b_4	$g_1\cdot10^5$	$g_2\cdot10^4$	g_3	g_4	g_5	$g_6\cdot10^4$	
Unit	MPa^{-4}	MPa^4	MPa^{-4}	MPa^{-2}	MPa^2			MPa^{-4}	
Value	7.0	1.8	2.6	3.0	0.65	0.346	0.36	7.0	
Fatigue model parameters									
Parameter	σ_0	a	C	$K\cdot10^5$	L_1	L_2	ϑ	c	Q
Unit	MPa							MPa^{-1}	MPa^{-1}
Value	3.5	0.075	2.7	5.0	150	149	6000	0.03	0.0054
Parameter	$Q_b\cdot10^4$	L_3	L_4	ϑ_2	$\mathcal{N}\cdot10^{10}$	q			
Unit	MPa^{-2}	MPa	MPa	MPa					
Value	2.5	33	74	1600	1.2	2.45			

approaches for fatigue (cumulative damage and cycle-counting approaches), in this approach, the movement of the endurance surface and damage evolution are determined in terms of stress increments, not in terms of stress cycles [34, 35, 36]. For this reason, this approach is well suitable for random 3D loadings. The evolution of damage obeys the $[1-D]$ damage concept by Lemaitre and Chaboche [26] including the loading history in the LCF regime [33].

The basis of improving the endurance function β is the well-known Gerber's rule (1874) for metals, which is modified for polymers to be

$$\sigma_\mathrm{a} = \sigma_{-1}\big(1-\zeta_1\big(\frac{\sigma_\mathrm{m}}{\sigma_\mathrm{u}}\big)^{\zeta_2}\big), \tag{6}$$

where σ_u is the peak yield stress (negative in compression). The parameters used are $\zeta_1 = 1.5$ and $\zeta_2 = 1.3$ (in the original Gerber's rule (1874), $\zeta_1 = 1.0$ and $\zeta_2 = 2.0$). The proposed endurance surface and its movement are discussed in Holopainen et al. [33]. The proposed endurance surface $\beta = 0$ under uniaxial loads simplifies to $\sigma_\mathrm{a} = \sigma_{-1} - g_\mathrm{I} = \sigma_{-1} - a\sigma_\mathrm{m} + a_1(\sigma_\mathrm{m})^2$ (cf. [34] for steels, where $\sigma_\mathrm{a} = \sigma_{-1} - a\sigma_\mathrm{m}$), where $a_1 = ac$ and σ_{-1} is the fatigue strength as $R = -1$ (equals to σ_0 as fatigue stops generating). The comparison between this 1D endurance surface and Gerber's rule (6) shown in Fig. 3 reveals that they are close in tension, but the linear term $a\sigma_\mathrm{m}$ (aI_1 in three dimensions) is mandatory under compression to obtain sufficiently large fatigue strengths, that is, the fatigue strengths under compression are significantly greater than those under tension.

The total number of fatigue model parameters is fifteen, and their values were extracted from eight tests [33], see Table 1. Even though the number of parameters appears to be high, they are required, and simpler empirical models [26] are not accurate to reproduce fatigue lives from the LCF region to the HCF region under different loading modes due to the complex ratcheting behavior arising from amorphous microstructure.

RESULTS

The distribution of the predicted shear strain (after 50 cycles when $\tau = \tau_\mathrm{min}$, $f = 1$ Hz, $R = 0.1$, and the maximum shear stress is 50 % of the ultimate shear strength, 40 MPa) in high-quality torsion specimens without notable imperfections is shown in Fig. 3 (simulated by Abaqus/implicit). As described in the standard ASTM D638 [37] for the geometry of the specimens, the response in the specimens' web (gauge section) remains homogeneous prior to rapid rupture. This outcome allows us to perform the forthcoming simulations in a single material (integration) point representative of

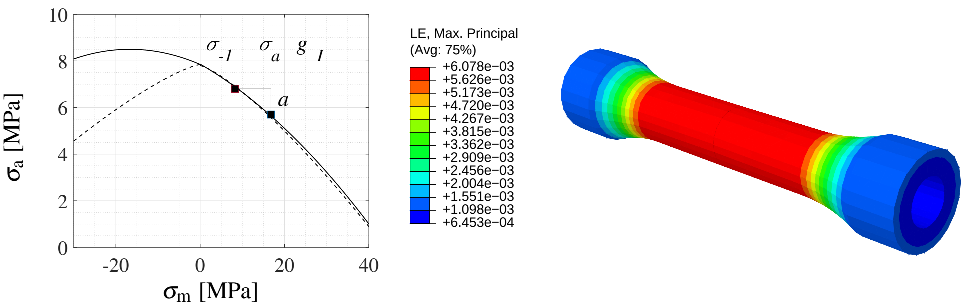

FIGURE 3. Stress amplitude vs mean stress for 60,000 cycles (Haigh-diagram) using the proposed model (black solid) and the modified Gerber's rule (6) (dashed) (left). Markers ■ denote the data points. In one dimension, $g_1(\sigma_{\rm m};a,a_1) = a\sigma_{\rm m} - a_1(\sigma_{\rm m})^2$. Finite element simulations for torsion (right). Pure shear prevails and thus, LE=LE12.

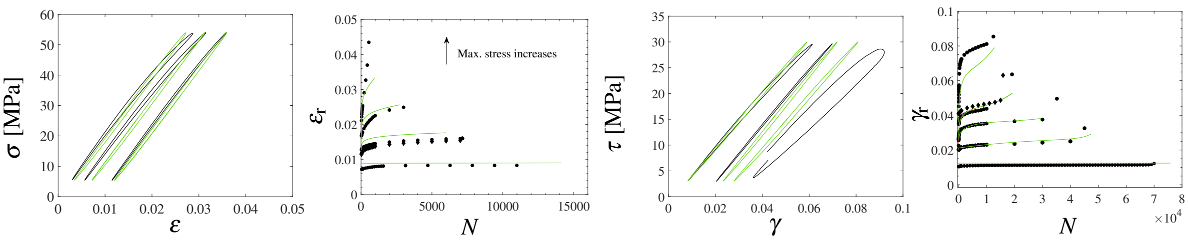

FIGURE 4. The 30th, 300th, and 3000th loops under uniaxial tension at $f = 5$ Hz and $R = 0.1$ (left). The black and green colors denote the data and model results. Corresponding ratcheting strains [33] (2nd from the left). The markers • denote data. The maximum stress levels applied are 50 %, 75 %, 90 %, and 97 %. Torsional test (black) and model (green) results for the maximum stress 75 % of the ultimate shear strength ($f = 1$ Hz and $R = 0.1$) (3rd from the left). The 30th, 10,000th, and 19,000 (before rupture of the specimen) cycles are shown. Shear ratcheting responses for the maximum stresses 82.5 %, 75 %, 65 %, 50 %, and 30 % of the ultimate strength [33] (right). The marker ◆ denotes another data which differs the most from the used most relevant data. Extracted from [33].

the specimen's web (prior to rapid rupture). This is a significant advantage when simulating resource-intensive long fatigue lives.

Tension

Fig. 4(left) shows hysteresis loops when the maximum stress is close to the peak yield stress of 60 MPa. The hysteresis loops show apparent ratcheting strain (also termed cyclic creep) as the load ranges between its minimum and maximum [3, 17, 25]. The ratcheting strain $\varepsilon_{\rm r}$ is defined as the mean value of the maximum strain $\varepsilon_{\rm max}$ and minimum strain $\varepsilon_{\rm min}$ in each cycle. In the subsequent figures, the predictions stop when full damage ($D = 1$) is achieved (prior to rupture of the specimens).

Regarding the ratcheting at the highest load level in Fig. 4(2nd from the left), the experimental response quickly grows and becomes greater than the model response after 100 cycles. The intense growth of the measured ratcheting strain is due to a mechanism of brittle failure including the scission of the polymer chains [38], which characteristic is not completely governed by the plasticity and fatigue damage models proposed. At the lower stresses, the model predicts the ratcheting strains and fatigue lives sufficiently accurately.

Torsion

The torsional ratcheting strain $\gamma_{\rm r}$ is defined as the mean value of the maximum shear strain $\gamma_{\rm max}$ and minimum shear strain $\gamma_{\rm min}$, respectively, in each cycle. Consider first the maximum stress levels of 75 % of the ultimate shear strength, 40 MPa. The predicted loops up to 10,000 cycles are close to the experimental ones, as depicted in Fig. 4(3rd from the left). As failure starts to influence, the measured ratcheting strain shows an increase, and the stiffness of the material

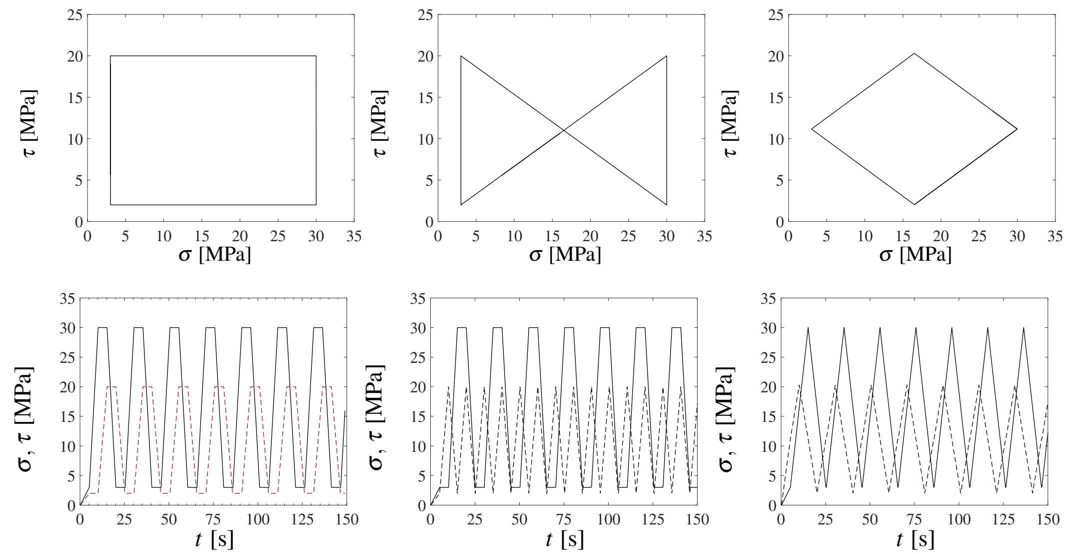

FIGURE 5. Load paths used in the multiaxial tests: τ vs σ (upper) and τ, σ vs time (lower; axial and shear stresses are separated by the solid and dashed curves). The symbols σ and τ mean the axial and shear stresses, respectively.

reduces and the area of the hysteresis loops grows (indicating a decrease in mechanical energy). The model is not able to predict this behavior since the stress and the fatigue damage are regarded as uncoupled, and consequently, on the microstructural basis, the predictions comply with permanent chain deformation rather than polymer chain breakage. However, as shown in Fig. 4(right), the loss of mechanical energy and chain breakage actually commence once the majority of the service life (over 90 %) has been passed. Therefore, despite the shape of the predicted load cycles prior to rupture may differ from that observed, the model predicts the ratcheting strains and fatigue lives well.

Multiaxial loads

The load paths applied are demonstrated in Fig. 5. To describe multiaxial loads in one dimension, the shear ratcheting strain γ_r defined previously is replaced by the equivalent ratcheting strain $\gamma_{er} = \gamma_r/\sqrt{3}$ [21].

First addressing the details of the squared load path demonstrated in Fig. 6. The predictions based on the improved rule (1) clearly evidence the accuracy in the model result. Owing to the rather long-lasting holding time applied (the duration of cycles is 20 seconds), the test also services to detect some static creep (at the maximum stresses) and recovery (at the minimum stresses). Interestingly, neither the test results nor the model manifest distinct creep or recovery under torsion, while they both are notable under tension. This result designates that the amorphous structure well resists creep and recovery under torsion. The developments of the fatigue damage and free volume are demonstrated in Fig. 6(middle); it is the fatigue damage that finally determines the fatigue life. The damage gradually grows which characteristic is owing to the canonical $[1-D]$ damage concept applied in this approach. This characteristic is intrinsic to many ductile materials and represents in APs fracturing of fibrils resulting in accumulated void volume fraction and microcracking [19, 20]. It is likely that the combined development of the free volume and fatigue damage, defined by $(D+\varphi/\varphi_{cv})/2$, resembles closely the development of the void volume accumulated by the void number density [39].

When investigating butterfly-type loads, the macroscopically observed ratcheting strains increase the most during the first thousands of load cycles, as shown in Fig. 7(right). This material behavior represents strong tertiary cyclic creep, and the ratcheting deformation (especially shear) shows a remarkable increase once 90 % of the fatigue life has been passed, defining the fatigue life.

In all the three multiaxial load cases applied, both the data and predictions show rapidly growing initial ratcheting strains (primary cyclic creep), which then progressively attain their stabilized values (secondary cyclic creep) after quite a small number of cycles. The butterfly-type load path resulted in the most high increase in ratcheting deformation before rupture, i.e., tertiary cyclic creep seems to be enhanced under combined tension and torsion when torsion in relation to the axial stress is rather small during the load cycles.

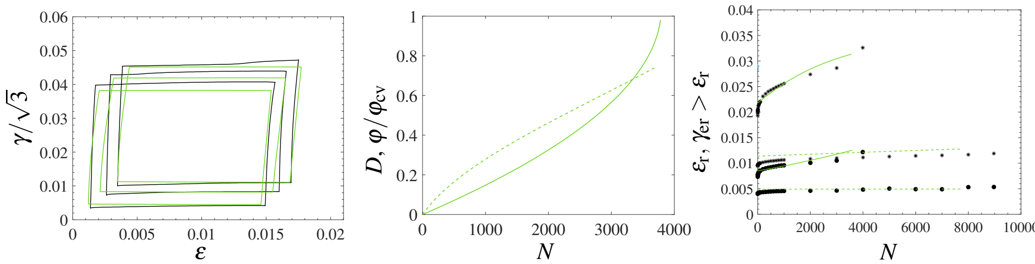

FIGURE 6. The measured (black) and predicted (green) 100th, 1000th, and 3500th (90 % of the fatigue life) cycles for the squared loads when the maximum axial and shear stresses are 50 % of their strengths [33] (left). Fatigue damage D (solid) and free volume (dashed) (middle). Predicted axial and shear ratcheting strains when the maximum stress levels are 50 % (solid) and 30 % (dashed) (right). The markers $\bullet$ and $*$ mean the corresponding data. Extracted from [33].

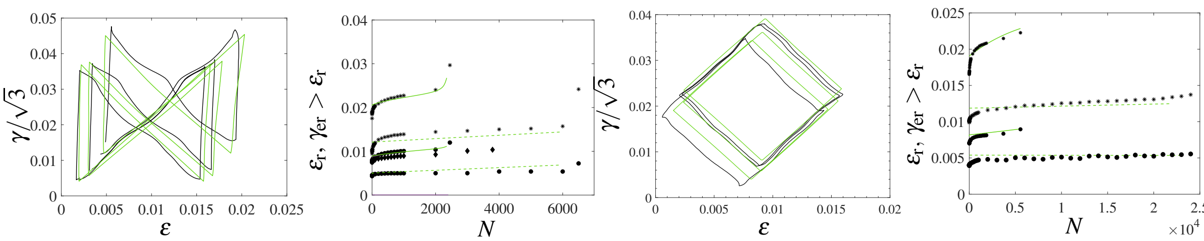

FIGURE 7. Measured (black) and predicted (green) axial strain vs shear strain for the butterfly-type loads when the maximum stresses are 50 % of their strengths [33] (left). The 100th, 1000th, and 2400th (just prior to rupture) cycles are shown. Predicted axial and shear ratcheting strain responses when the maximum stress levels of 50 % (solid) and 30 % (dashed) are applied (2nd from the left). The markers $\bullet$ and $*$ mean the corresponding data, and $\blacklozenge$ indicates another data which differs the most from the used data. Axial strain vs shear strain for the corresponding rhombic load [33] (3rd from the left). The 100th, 1000th, and 5000th cycles are shown. Measured and predicted axial and shear ratcheting strains (rhombic) (right). Extracted from [33].

CONCLUSION

The main conclusions were as follows: [i] The amorphous polymer structure firmly resists static creep and recovery under torsion. [ii] However, the amorphous structure exhibits more ratcheting in torsion than in tension. Nevertheless, the amorphous structure appeared to well resist fatigue damage under cyclic torsion. [iii] The ratcheting strains do not increase notably until 90 % of the fatigue life is achieved and, that is, ratcheting deformation is an important precursory indicator for the drastic damage of structural components that may cause terrible accidents and huge financial losses. [iv] The free volume controls the development of plastic deformation and large ratcheting strains. [v] The free volume and fatigue damage developments significantly affect the tertiary cyclic creep at the end of the fatigue life, that is, they define the fatigue life. The combined development of the fatigue damage and free volume was found to be close to the development of void volume. Therefore, the fatigue life of PC-components could be increased by restricting the void volume development during their manufacturing: molding pressure and temperature, the size of the runner and gate of the mold, and use of suitable additives (impact modifiers). The results presented in this work can be used to enhance fatigue-resistant material development (APs) and to predict fatigue life of engineering components made of APs.

ACKNOWLEDGMENTS

This research has been supported by the EIPHI Graduate School (contract ANR-17-EURE-0002) including its experimental facilities.

REFERENCES

1. W. W. Adams, B. L. Farmer, and J. P. Haines, Mater. Today **1**, 25 (1998).
2. J. Wang, Y. Xu, W. Zhang, and Z. Moumni, Materials and Design **97**, 519 (2016).
3. G. Kang and Q. Kan, *Cyclic Plasticity of Engineering Materials: Experiments and Models* (John Wiley & Sons, Chichester, 2017).
4. Z. Lei and P. Wu, Nat. Commun. **10**, 3429 (2019).
5. S.-A. Park, H. Jeon, H. Kim, S.-H. Shin, S. Choy, D. S. Hwang, J. M. Koo, J. Jegal, S. Y. Hwang, J. Park, et al., Nat. Commun. **10**, 2601 (2019).
6. E. J. Frankberg, J. Kalikka, F. G. Ferrá, L. Joly-Pottuz, T. Salminen, J. Hintikka, M. Hokka, S. Koneti, T. Douillard, B. L. Saint, et al., Science **366**, 864 (2019).
7. M. C. Boyce, D. M. Parks, and A. S. Argon, Mechanics of Materials **7**, 15 (1988).
8. C. Dreistadt, A. S. Bonnet, P. Chevrier, and P. Lipinski, Materials and Design **30**, 3126 (2009).
9. S. Holopainen and M. Wallin, ASME J. Engng. Materials Technol. **135**, 1 (2012).
10. T. Barriere, X. Gabrion, and S. Holopainen, Int. J. Plasticity **122**, 31 (2019).
11. S. Holopainen, Mechanics of Materials **66**, 35 (2013).
12. S. Holopainen and T. Barriere, Computers and Structures **199**, 57 (2018).
13. G. Chen, H. Q. Liang, L. Wang, Y. H. Mei, and X. Chen, Polym. Eng. Sci. **55**, 664 (2015).
14. T. Barriere, X. Gabrion, S. Holopainen, and J. Jokinen, Int. J. Plasticity **135**, 102781 (2020).
15. L. Anand and N. M. Ames, Int. J. Plasticity **22**, 1123 (2006).
16. R. P. M. Janssen, D. K. Kanter, L. E. Govaert, and H. E. H. Meijer, Macromolecules **41**, 2520 (2008).
17. C. K. Jiang, H. Jiang, J. W. Zhang, and G. Z. Kang, Polym. Engngn. Sci. **55**, 2559 (2015).
18. A. Krairi, I. Doghri, J. Schalnat, G. Robert, and W. Van Paepegem, Int. J. Plasticity **115**, 154 (2019).
19. M. N. James, Y. Lu, C. J. Christopher, and E. A. Patterson, Engng. Fract. Mech. **108**, 89 (2013).
20. K. S. Ravi Chandran, Polymer **91**, 222 (2016).
21. F. Lu, G. Kang, Y. Zhu, C. Xi, and H. Jiang, Polymer Testing **50**, 135 (2016).
22. A. Krairi and I. Doghri, Int. J. Plasticity **60**, 163 (2014).
23. C. Xi, G. Kang, F. Lu, J. Zhang, and H. Jiang, Materials and Design **67**, 644 (2015).
24. M. J. W. Kanters, T. Kurokawa, and L. E. Govaert, Polymer Testing **50**, 101 (2016).
25. S. Holopainen, T. Barriere, G. Cheng, and R. Kouhia, Int. J. Plasticity **91**, 109 (2017).
26. J. Lemaitre and J. L. Chaboche, *Mechanics of Solid Materials.* (Cambridge University Press, Cambridge, 1999).
27. Abaqus, Tech. Rep., Dassault Systémes Simulia Corp., Providence, RI, USA (2014).
28. A. Cherouat, H. Borouchaki, and Z. Jie, Metals **8**, 1 (2018).
29. P. D. Wu and E. Van der Giessen, J. Mech. Phys. Solids **41**, 427 (1993).
30. M. C. Boyce, E. M. Arruda, and R. Jayachandran, Polym. Engngn. Sci. **34**, 716 (1995).
31. ASTM E2207, ASTM International pp. 1–8 (2002).
32. L. Anand and B. P. Gearing, Int. J. Solids Structures **41**, 3125 (2004).
33. T. Barriere, X. Gabrion, and S. Holopainen, Int. J. Plasticity **147**, 103106 (2021).
34. N. Ottosen, R. Stenström, and M. Ristinmaa, Int. J. Fatigue **30**, 996 (2008).
35. S. Holopainen, R. Kouhia, and T. Saksala, European Journal of Mechanics A/Solids **60**, 183 (2016).
36. T. Frondelius, S. Holopainen, R. Kouhia, N. Ottosen, M. Ristinmaa, and J. Vaara, MATEC Web Conf **300**, 16008 (2019).
37. ASTM D638, ASTM International pp. 1–15 (2003).
38. F. J. Vernerey, R. Brighenti, R. Long, and T. Shen, Macromolecules **51**, 6609 (2018).
39. A. L. Bowman, S. Mun, S. Nouranian, B. Huddleston, S. Gwaltney, M. Baskes, and M. Horstemeyer, Polymer **170**, 85 (2019).